Bionanocomposites with Enhanced Physical Properties from Curli Amyloid Assemblies and Cellulose Nanofibrils

Vinay Khatri[1,2,3]†, Maziar Jafari[1,]†, Marc Beauregard[4,5], Mohamed Siaj[1], Denis Archambault[2,]*, Éric Loranger[5,6,]*, and Steve Bourgault[1,3]*

[1]*Department of Chemistry, Université du Québec à Montréal, C.P. 8888, Succursale Centre-Ville, Montreal, Quebec H3C 3P8, Canada*
[2]*Department of Biological Sciences, Université du Québec à Montréal, C.P. 8888, Succursale Centre-Ville, Montreal, Quebec H3C 3P8, Canada*
[3]*Québec Network for Research on Protein Function, Engineering and Applications, PROTEO, Montreal, Quebec H3C 3P8, Canada*
[4]*Department of Chemistry, Biochemistry and Physics, Université du Québec à Trois-Rivières, 3351 Des Forges, Trois-Rivières, Quebec G8Z 4M3, Canada*
[5]*Innovations Institute in Ecomatériaux, Ecoproduits et Ecoenergies (I2E3), Université du Québec à Trois-Rivières, 3351 Des Forges, Trois-Rivières, Québec G8Z 4M3, Canada*
[6]*Department of Mechanical Engineering, Université du Québec à Trois-Rivières, 3351 Des Forges, Trois-Rivières, Quebec G8Z 4M3, Canada*
†These authors contributed equally

Corresponding authors

Denis Archambault, C.P. 8888, Succursale Centre-Ville, Montréal, H3C 3P8, Canada;
e-mail address: archambault.denis@uqam.ca

Éric Loranger, 3351 Des Forges, Trois-Rivieres, Quebec, Canada
e-mail address: eric.loranger1@uqtr.ca

Steve Bourgault, C.P. 8888, Succursale Centre-Ville, Montréal, H3C 3P8, Canada;
e-mail address: bourgault.steve@uqam.ca

ABSTRACT: Proteinaceous amyloid fibrils are one of the stiffest biopolymers owing to their extensive cross-β-sheet quaternary structure whereas cellulose nanofibrils (CNFs) exhibit interesting properties associated with their nanoscale size, morphology, large surface area, and biodegradability. Herein, CNFs were supplemented with amyloid fibrils assembled from the Curli-specific gene A (CsgA) protein, the main component of bacterial biofilms. The resulting composites showed superior mechanical properties, up to 7-fold increase compared to unmodified CNF films. Wettability and thermogravimetry analyses demonstrated high surface hydrophobicity and robust thermal tolerance. Bulk spectroscopic characterization of CNF-CsgA films revealed key insights into the molecular organization within the bionanocomposites. Atomic force microscopy and photo-induced force microscopy revealed the high-resolution location of curli assemblies into the CNF films. This novel sustainable and cost-effective CNF-based bionanocomposites supplemented with intertwined bacterial amyloid fibrils opens novel directions for environmentally friendly applications demanding high mechanical, water-repelling properties, and thermal resistance.

KEYWORDS: Biocomposites, amyloid fibrils, nanocellulose, curli, curli-specific gene A; protein filaments

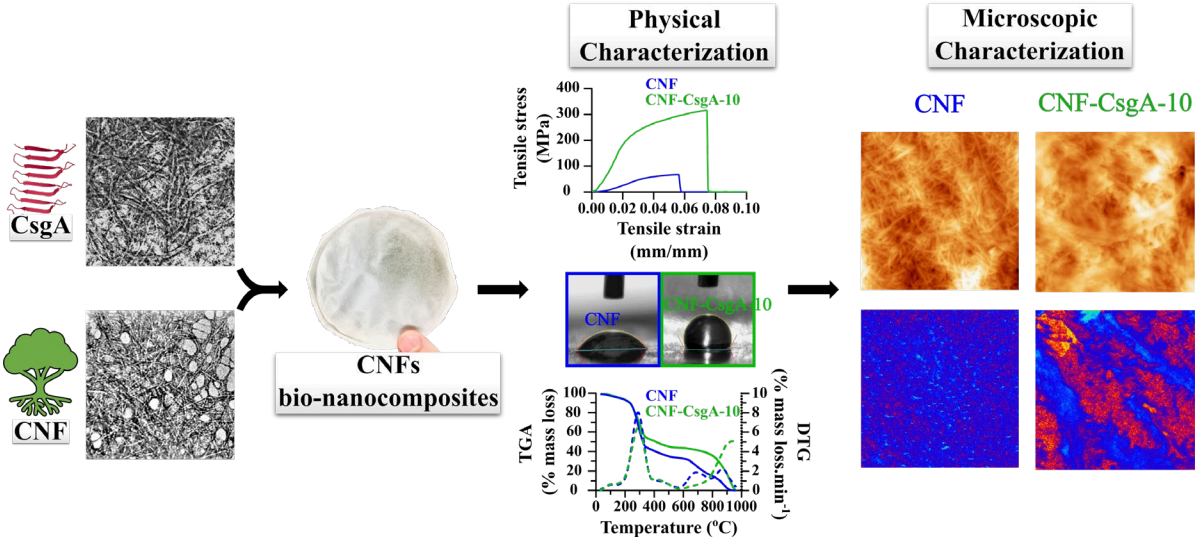

Graphical abstract

INTRODUCTION

Due to increasing environmental concerns associated with the widespread accumulation of non-biodegradable synthetic polymers, composites based on biological materials have received increased interest for numerous applications owing to their sustainability and renewability[1]. Among constituents that could be used for the fabrication of renewable biocomposites, materials assembled from polysaccharides and proteins have shown interesting chemical, physical and mechanical properties[2]. Notably, proteins are well-known for their unique ability to self-associate into supramolecular structures and the resulting organized nanomaterials have remarkable characteristics that are exploited by all living organisms[3]. For instance, insect silks and collagen originated from vertebrates have been an important source of inspiration for the fabrication of proteinaceous materials than can be integrated into composites. Interestingly, discoveries of the last two decades revealing that amyloid fibrils perform vital biological activities in host organisms have prompted their usage as biomaterials[4]. While amyloid structures have been historically associated with diseases[5], today, functional amyloids have been identified in almost all species, from bacteria to humans[6]. Amyloid fibrils are linear and unbranched proteinaceous filaments of 3 to 10 nm in diameter and 0.1-10 μm in length, characterized with a cross-β-sheet quaternary organization in which the β-strands are oriented perpendicularly to the fibril axis[7]. This supramolecular organization involving an extensive network of hydrogen bonds between β-strands confers to the filaments high elastic moduli in the order of 3-20 GPa[8], identifying them as one of the stiffest protein biopolymers[9]. Additionally, in contrast to soluble proteins, amyloid fibrils are resistant to thermal denaturation and proteolytic degradation[10]. Amyloids originating from biological sources are also cost-effective, eco-friendly and easy to access and to scale-up[11]. These properties indicate that amyloid fibrils could be a promising renewable constituent material for

biocomposites, as recently exemplified with their combination with polysaccharides to generate reinforced materials[12, 13].

Amongst polysaccharides used for the fabrication of biocomposites, cellulose nanomaterials (CNMs) exhibit interesting properties associated with their nanoscale size, fibril morphology, large surface area, mechanical strength, biocompatibility and biodegradability[14]. In fact, CNMs are currently being evaluated as constituents of composites and polymer reinforcements for applications in electronics, textiles, and health[14, 15, 16]. CNMs encompass a large array of nanoscale cellulose-based particles having various shapes, sizes, and surface chemistries. Among CNMs, cellulose nanofibrils (CNFs), also known as nanofibrillated cellulose (NFC), are of particular interest for their straightforward and cost-effective production, sustainability, ease of functionalization and strength resulting from extensive hydrogen bonding[16]. While individual CNFs demonstrate elastic moduli values in the hundreds of GPa[17], the mechanical robustness of CNFs is not the determining factor defining the strength of resulting macroscopic materials. In fact, in addition to physical contributions of individual CNFs, interactions between fibrils constitute a critical factor determining the overall strength of the material[18], as exemplified with the 100-fold more fragile CNF films, compared to the unitary CNF constituents[19, 20]. Thus, having a constituent additive to increase the mechanical properties of CNF-based thin films remains important in the context of engineering renewable biocomposites[21].

Recently, CNMs and proteinaceous amyloid fibrils have been combined to generate biocomposites in the form of films and hydrogels[20, 22, 23]. For instance, bio-sorbent films prepared from CNFs and lysozyme amyloid fibrils were shown to be highly efficient to remove mercury from water, in addition to a noticeable physical reinforcement of the CNF films [23]. Moreover, CNC (Cellulose NanoCrystal) or CNF films supplemented with hen egg lysozyme protein, under the

monomeric and fibrillated states, showed improved mechanical properties (tensile strength, toughness), albeit the improvement remains somewhat moderate[20, 23]. While these reports highlight that the addition of cross-β-fibrils into CNM-based composites could be beneficial to improve mechanical properties, the protein used in these studies, *i.e.,* lysozyme, bovine serum albumin (BSA) and β-lactoglobulin, are not amyloidogenic *per see* and need to be subjected to harsh conditions (T°, extreme pH) to denature the native structure and to force aggregation. Using naturally occurring amyloidogenic proteins with robust self-assembling properties and high propensity to form intertwined fibril networks could lead to enhanced improvement of the overall mechanical performance of the resulting biocomposites. Herein, we investigated the incorporation of amyloid fibrils assembled from a highly amyloidogenic-prone protein originating from bacterial curli fibrils[24] into CNFs to generate nanocomposites. CNFs were mixed with curli amyloids to fabricate thin films, leading to materials with improved mechanical properties, thermal stability, and surface water-repelling features. Advanced spectroscopic and optical characterization revealed the distribution and the organization of curli amyloid fibrils within the CNF films. Overall, this study revealed that curli amyloid fibrils originating from bacterial biofilms could be exploited as potent reinforcing constituent for cellulose-based films.

EXPERIMENTAL SECTION

Fabrication of CNFs. CNFs were produced using a commercial never-dried bleached kraft hardwood pulp through 4-acetamido-2, 2, 6, 6-tetramethyl-1-piperidinyloxy (TEMPO) oxidation and mechanical dispersion, as previously described[25].

Peptide Synthesis, Purification, and Characterization. Peptides were synthesized on a solid support using Fmoc-chemistry and 2-(6-chloro-1-H-benzotriazole-1-yl)-1, 1, 3, 3-tetramethylaminium hexafluorophosphate (HCTU) coupling strategy with the incorporation of oxazolidine pseudoproline derivatives to facilitate synthesis, as previously described[26]. After acidic cleavage, purification by reverse phase HPLC and characterization by mass spectroscopy, peptides were filtered through a 0.22 μm hydrophilic filter and lyophilized. Peptides were kept dried at -80 °C until used. Peptide concentrations were validated by measuring absorbance at 280 nm using theoretical molar extinction coefficients and by measuring the area under the curve at 229 nm obtained by reverse phase HPLC.

Expression and Purification of CsgA. His-tagged CsgA (GenBank Accession WP_124055573) was expressed in NiCo21 (DE3) competent *Escherichia coli*, as recently described[27]. After 1h induction with IPTG, cells were harvested by centrifugation and kept at -80 °C until lysis and purification. All purification steps were performed under denaturing conditions (8 M GdnHCl) to prevent any undesired aggregation, until initiation of self-assembly by exchanging buffer to 1× PBS pH 7.4 buffer. CsgA was purified by affinity chromatography over a Profinity™ IMAC Ni-Charged equilibrated in 1× PBS pH 7.2, 8 M GdnHCl. CsgA was eluted using 250 mM imidazole in 1× PBS pH 7.4 buffer. A final desalting step was performed using a Sephadex G-25 fine 20-80 μm mesh in a spin desalting column in 1× PBS pH 7.4 buffer.

Purified protein solutions were sterilized using 0.22 μm filters. Purity was assessed by SDS-PAGE and concentration was quantified by the micro BCA™.

Self-assembly into Amyloid Fibrils. For IAPP and I_{10} assembly, peptide solutions were incubated in 20 mM Tris-HCl buffer (pH 7.4) for up to 5 days at room temperature without agitation[28] and under circular agitation at 40 rpm[29], respectively. CsgA protein was assembled at 0.6 mg/mL in 1× PBS buffer (pH 7.4) without any tumbling at RT for up to 48 h[27]. During the self-assembly process, mixtures were periodically analyzed by circular dichroism, fluorescence spectroscopy, as well as atomic force and transmission electron microscopy.

Fabrication of CNF-amyloid Bionanocomposites. A 50 mL CNF suspension at a concentration of 0.5% (w/v) was mixed, or not, with different amounts of peptide and protein. The CNF:protein mass ratio and wt% values are indicated in **Table S1**. The mixture was stirred for 30 minutes at room temperature at a low speed to prevent air bubble formation in the solution. The solution was then poured into a 90 mm diameter aluminum dish followed by air drying at controlled humidity of 50% for 4 days[25, 30, 31]. The produced CNFs, without protein, had a carboxyl content of 1 700 $mmol.kg^{-1}$. To prevent variability caused by acidic/basic pH, all film formation solutions were close to neutral (pH = 7.4). At this pH, CNF (pKa ~ 4) is negatively charged. The theoretical pI of BSA and CsgA are respectively ~ 4.7 and ~ 4.9, making them also negatively charged at pH 7.4. The ionic strength of the dispersion was determined to be 56 mM[32].

Circular Dichroism Spectroscopy. A Jasco J-815 CD spectrometer was used to record Far-UV CD spectra from 190 to 260 nm at RT. The wavelength step was set at 0.5 nm with a scan rate of 20 $nm.min^{-1}$. Spectra were background subtracted with buffer (1× PBS pH 7.4). The spectra and raw data were converted to mean residue ellipticity (MRE).

Fluorescence Spectroscopy. A PTI QuantaMaster spectrofluorometer was used for fluorescence measurements. IAPP, I_{10} and CsgA solutions were diluted to reach a concentration of 50 μM, in presence of 40 μM ThT. Emission from 450 nm to 550 nm was recorded with an excitation wavelength of 440 nm. For 8-anilino-1-naphthalenesulfonic acid (ANS), 50 μM of ANS was used and the fluorescence emission was measured between 385 nm and 550 nm with constant excitation at 370 nm. Fluorescence was measured in quartz ultra-micro cells of 10 mm in length. Data are the average of at least 3 different individual experiments.

Attenuated Total Reflection-Fourier Transform Infrared Spectroscopy. ATR-FTIR spectra were recorded at RT using a Nicolet 6700/Smart iTR spectrometer equipped with a DTGS-KBr detector in the range of 4000-650 cm^{-1}. Each spectrum was an average of 64 scans recorded at a resolution of 2 cm^{-1} using a Happ–Genzel apodization.

Mechanical Properties. A tensile instrument (Instron 4201™) equipped with a 500 N load cell was used to measure Young's modulus (stiffness), tensile stress (tensile strength), strain at a maximum load (strain-to-failure) and strain energy (toughness) of CNF films, as described elsewhere[25, 31]. Briefly, rectangular sections of 8 cm × 1 cm of dry CNF films were stretched at a rate of 10 mm/min. All the stress-strain curves were recorded at 25 °C and 50% relative humidity. The thickness of the samples was measured with a Lhomargy™ micrometer.

Contact Angle Analysis. Contact angle measurements (FTA4000, First Ten Angstroms) were carried out to evaluate the hydrophobicity of the film surface. At least 5 drops (0.8 μL ± 0.07) of water were deposited onto each substrate and a total of 300 images were captured within 5 s for each drop. The contact angle reported was for the second image, therefore at 6.7 ms. The contact angle was determined by measuring the angle between the sample surface and the tangent at the droplet solid-liquid-air point using a contact angle system OCA20, as described[25].

Atomic Force Microscopy. Peptide and CsgA assemblies were respectively diluted in 1% acetic acid and immediately applied to freshly cleaved mica. The mica was washed twice with deionized water and air-dried for 24 h. Samples were analyzed using a Veeco/Bruker Multimode8 AFM. For bionanocomposites, a 1 cm × 1 cm section of dry CNF films was cut and mounted on a magnetic sample holder via double-sided carbon tape. The Multimode8 scanning probe microscope (SPM) running ScanAssyst^{TM} program, optimizing non-contact (NC) and contact (C) modes, was used to capture topographic information of the sample surfaces. The scan frames were 1 μm × 1 μm and the images were recorded at 1 line/s for a total resolution of 512 lines/scan. The probe was a silicon nitride (Si_3N_4) cantilevered tip with a 2-12 nm nominal radius. AFM images were treated using the open-access SPM software WSxM.

Transmission Electron Microscopy. Peptide and CsgA assemblies were diluted in Tris-HCl before being applied to glow-discharged carbon films on 400 μm mesh copper grids. After adsorption, samples were negatively stained with 1.5% uranyl formate for 1 min and air-dried for 15 min. Images were recorded using a FEI Tecnai 12 BioTwin microscope. For the CNF mixture, the samples were prepared by depositing drops of 0.001% CNF suspensions on carbon-coated electron microscope grids and negatively stained with 1.5% uranyl formate. Following this, the grids were air-dried and observed with a Philips EM208S transmission electron microscope.

X-ray Photoelectron Spectroscopy (XPS). CNF dry films were cut into 2 cm × 2 cm pieces for XPS analyses. The Escalab 250Xi XPS instrument was used to conduct elemental characterization on the first 10-20 nm of the CNF and CNF-protein blended films. The pressure in the chamber was 1.0×10^{-7} Torr. The X-ray source was a monospectral Al Kα 1486.68 eV powered at 218.8 W (14.7 kV and 14.9 mA). The electron emission angle was 0 degrees. Survey maps were recorded from 0 to 1351 eV (± 1.0 eV) and high-resolution spectra of C_{1s} from 278.7 to 296.7 eV,

O_{1s} from 526.7 to 543.7 eV and N_{1s} from 391.7 to 411.7 eV (± 0.1 eV) were collected on areas of 650 μm^2.

Scanning Electron Microscopy/Energy Dispersive X-ray Spectroscopy (SEM/EDXS). SEM and EDXS of CNF bionanocomposites were taken with JSM-7600-F (JEOL) and a Silicon Drift Detector (SDD) (Oxford Instruments) X-MAX 80 mm^2, respectively. The measurements were done with a beam acceleration voltage of 12 keV under low current conditions in a 10^{-6} Torr vacuum. The EM detector was a lower, or in-chamber, secondary electron detector. A 1 cm × 1 cm section of dry CNF films was cut and mounted on a magnetic sample holder via double-sided carbon tape and placed in the SEM at a working distance of 7.1 mm. A semi-quantitative elemental characterization 500 nm – 2 μm deep into the sample was performed on a 0.1 mm^2 area scan of each sample by EDXS to assess the nitrogen element content.

Photo-Induced Force Microscopy (PiFM). Topography, chemical contrast PiFM images, and point-spectral information were obtained by the VistaScope scanning probe microscope. The probe was a 30-40 nm diameter Au-coated cantilever tip. A 1 cm × 1 cm section of dry CNF films was cut and mounted on a magnetic sample holder. For the topography images, a 1 μm × 1 μm scan frame was scanned at 1 line/s with a resolution of 256 lines/scan. PiFM chemical contrast images were recorded by scanning the sample at wavelengths of interest, determined by the peaks in the point spectra. The same scan rate, scan size and resolution were retained for the PiFM measurements. Each 1 μm × 1 μm scan frame was probed at 5 points separated equidistantly on a diagonal line for the point spectra. The spectra were taken in 30 seconds with a resolution bandwidth of ~0.5 cm^{-1} and ranged in the mid-infrared spectrum from 770 to 1910 cm^{-1}. They were then averaged for the chemical signature of each film. To highlight compositional differences between the CNF/amyloid composite films, a pair of point spectra were targeted in an area of clear

chemical contrast and the differences in intensities were observed. Images were processed with the open-access SPM software WSxM[33].

Thermal Gravimetric Analysis. For thermal stability analyses and hydration properties, the Q5000 (TA instruments) was operated to heat ~4 to 6 mg of each CNF film from 30°C to 960°C at a rate of 20°C/min. The film dehydration experiments were conducted isothermally at 110°C for 20 min, with a temperature ramp of 20°C/min starting from 30°C. Both experiments were performed under normal pressure and in an inert atmosphere through a constant influx of Ar.

Statistical Analysis. Statistical analyses were performed using unpaired Student's parametric t-test with a 95% confidence level and a significant statistical difference was established at $p < 0.033$ (*); $p < 0.002$ (**); $p < 0.001$ (***). Statistical analyses were carried out using GraphPad Prism 8.0 software.

RESULTS AND DISCUSSION

Design of CNF-based films Supplemented with Amyloid Fibrils. To investigate the effects of the addition of amyloid fibrils derived from bacterial biofilms on the mechanical and physicochemical properties of the resulting cellulose-based biocomposite, CNF films supplemented with filaments assembled from the recombinant curli protein were prepared. Owing to its strong self-assembling properties and the mechanical robustness of the resulting fibrils, the protein Curli-specific gene A (CsgA)[24] was targeted. CsgA is the primary protein component of enteric bacteria biofilms[34] and its filaments offer structural support for the colonization of tissues and inert surfaces[35]. Recombinant CsgA monomers readily self-assemble into long, unbranched and intertwined fibrils with comparable (supra)structural architecture to their bacterial counterparts[36]. The extensive intermolecular hydrogen bond ladders involving Asn/Gln and backbone amide groups confer high stability to the supramolecular organization[24]. Interestingly, it has been observed that CsgA conferred substantial mechanical improvements over alginate-based hydrogels[13]. To evaluate the importance of the intertwined organization of CsgA filaments and their known capacity to adhere to inert surfaces on the properties of the resulting bionanocomposites, we also prepared CNF films supplemented with amyloid fibrils assembled from synthetic peptides, *i.e.* from the aggregation-prone peptide hormone amylin (islet amyloid polypeptide (IAPP))[37] and a 10-mer peptide derived from IAPP (I_{10}; SNNFGAILSS)[26]. IAPP is a 37-residue peptide hormone whose tissue deposition in the pancreatic islets of Langerhans is associated with type II diabetes[38]. The peptide I_{10} consists of the 20-29 segment of IAPP and has a high propensity to self-assemble into twisted fibrils rich in cross-β-sheet quaternary structure[26, 39]. BSA and milk protein were used as non-assembled protein control in the fabrication of the

bionanocomposites. A schematic representation of the experimental workflow is summarized in **Figure S1**.

Preparation and Characterization of Amyloid Fibrils. Recombinant CsgA was expressed in *E. coli* and purified by affinity and size exclusion chromatography, leading to a highly pure solution, as observed by SDS-PAGE analysis showing a single band at a molecular weight of ~15 kD (**Figure S2**). IAPP and I_{10} were obtained by solid-phase synthesis, purified by reverse-phase chromatography and identity/purity was confirmed by ESI-LC-MS (**Figures S3** and **S4**). CsgA was assembled at 0.6 mg/mL in 1× PBS buffer (pH 7.4) at RT for 48 h. IAPP was assembled at 50 μM in 20 mM Tris-HCl buffer (pH 7.4), whereas I_{10} fibrils were formed under the same conditions, but with continuous circular tumbling at 40 rpm. The self-assembly process was periodically analyzed by CD spectroscopy, ThT fluorescence, AFM and TEM. CD spectra indicated that immediately after purification, CsgA was largely unstructured. However, after quiescent incubation, CD spectra of CsgA displayed a characteristic minimum at ~218 nm and maximum at ~197 nm, corresponding to a β-sheet-rich secondary structure (**Figure 1a**). CsgA conformational transition to cross-β-sheet was probed by measuring ThT fluorescence, an amyloid-specific dye commonly used to assay fibril formation[40]. ThT emission increased over incubation time, indicative of the self-assembly of CsgA from an unstructured soluble protein into a cross-β quaternary structure (**Figure 1b**). As observed by AFM and TEM, CsgA assembled into a dense network of intertwined fibrils after 24 h of incubation, with fibrils having a diameter in the order of 1.5 - 5 nm (**Figures 1c** and **d**). Similarly, upon incubation in aqueous buffer, IAPP and I_{10} underwent a conformational transition associated with amyloid formation, as shown with the characteristic β-sheet secondary structure and the positive ThT signal (**Figures 1e, f, i** and **j**). IAPP and I_{10} assembled into polymorphic amyloid fibrils with the coexistence of twisted and helical

ribbon morphology with heights in the vicinity of 3 to 6 nm (**Figures 1g, h, k** and **l**). These observations agree with the typical morphological heterogeneities of filaments assembled with these polypeptides[26, 37, 41].

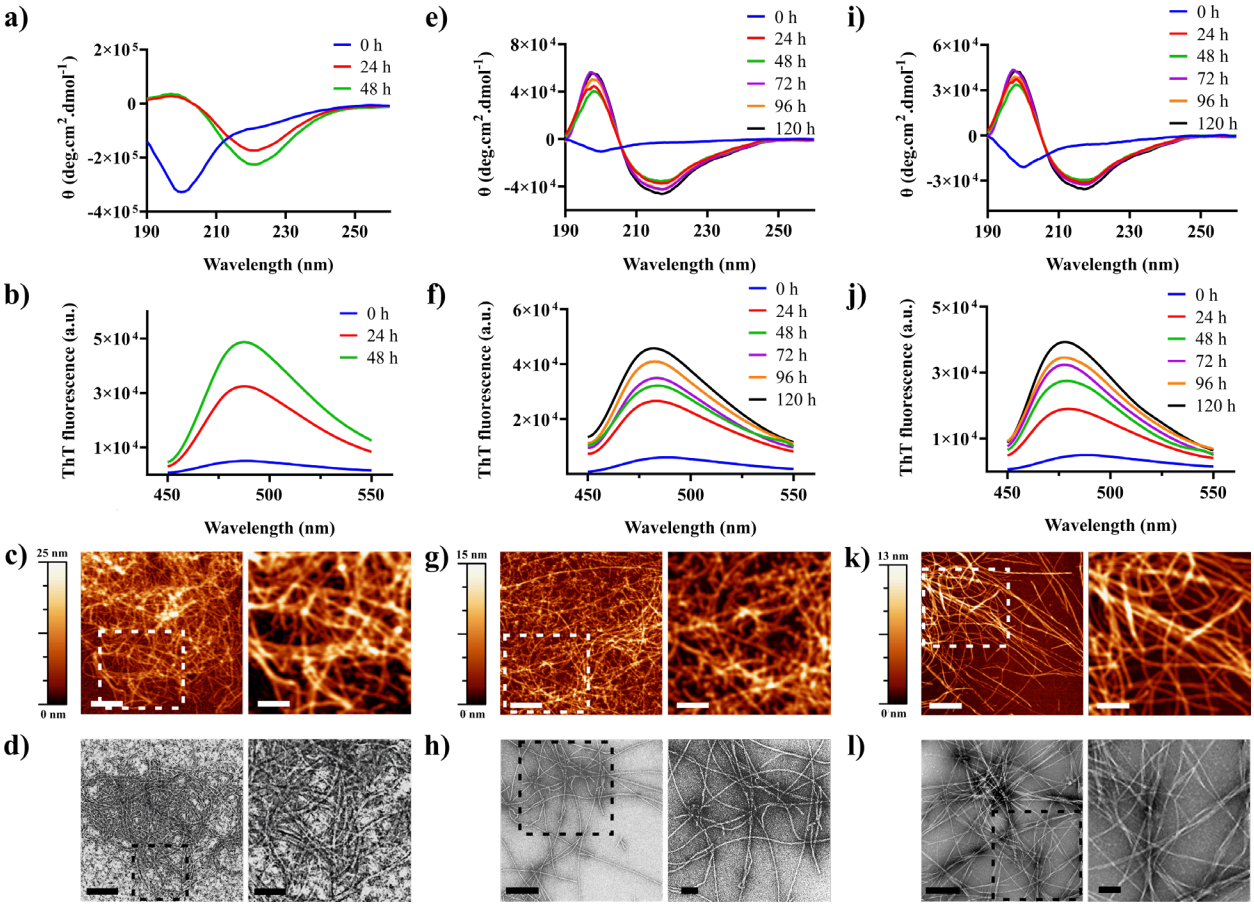

Figure 1. Self-assembly into cross-β-sheet amyloid fibrils. CD spectroscopy, ThT fluorescence, AFM and TEM characterization of CsgA (**a-d**), IAPP (**e-h**) and I_{10} (**i-l**) over incubation time. Scale bars are 500 nm and 250 nm for the AFM images and insets, respectively. Scale bars are 300 nm and 100 nm for the TEM images and insets, respectively.

Supplementing CNF Films with CsgA Fibrils Enhances Mechanical Strength. Firstly, CNFs were fabricated using 4-acetamido-TEMPO oxidation combined with mechanical dispersion[25, 30, 31]. TEM analysis of CNF materials revealed an average length of 176.8 ± 62.7 nm and an average diameter of 18 ± 9.5 nm for the nanofibrils (**Figure S5**). These measurements are

within range of the typical dimensions of TEMPO-treated CNFs[42], considering pulp sources alike[43]. Next, we fabricated CNF-based films supplemented with different proteinaceous materials, as described in the experimental section, and evaluated their mechanical properties using a typical stress-strain protocol. Each measurement generated a force-distance curve plotting the stress-strain curve (**Figure 2a** and **S6a**) to derive Young's modulus (stiffness) (**Figure 2b** and **S6b**), tensile stress (tensile strength) (**Figure 2c** and **S6c**), and strain energy (toughness) (**Figure 2d** and **S6d**). CNF films prepared in absence of protein additives showed comparable mechanical properties to other films reported in the literature, using similar sources of cellulose, but with different treatment methods (**Figure 2** and **Table S2**). BSA and milk proteins were used as control of proteinaceous additives in the fabrication of the CNF-based films. Results revealed no significant differences in the mechanical properties of BSA- and milk-supplemented CNF films compared to the CNF-only film (**Figure 2, S6** and **S7**). Similarly, in attempts to synchronize the process of amyloid assembly with CNF film formation during the drying process, recombinant CsgA and synthetic peptides were respectively added to CNF before their self-assembly, *i.e.,* under their monomeric and/or pre-fibrillar states. No significant improvements in the mechanical properties of the resulting CNF films were observed when non-assembled (monomeric and/or pre-fibrillar states) proteins were used (**Figure S7**).

In sharp contrast, when pre-assembled CsgA amyloid fibrils were introduced into the CNF matrix, substantial changes were observed **(Figures 2** and **S6**). The stress-strain curves of the CsgA-CNF bionanocomposites revealed that Young's modulus, tensile stress, strain-to-failure and strain energy were significantly higher than CNF control films (unmodified, BSA, milk protein) and these effects were dependent on the amount of CsgA loaded into the CNF films. For instance, when 0.4 wt % of CsgA was loaded into CNF films, the mean value of Young's modulus, tensile

stress at maximum load and strain energy showed prominent increases of 163%, 58% and 80%, respectively, compared to that of CNF alone (**Figure 2d**). When the CsgA loading was increased to 5 and 10 mg, *i.e.* 2 wt % and 4 wt %, the mean moduli were enhanced by 289% and 499%, respectively (**Figure 2**). It is also important to note that the negative charged CsgA (pI ~ 4.8) during film preparation at neutral pH most likely precluded its electrostatic-induced aggregation with the negatively charges CNFs (pKa of carboxylic acid ~ 4.0) during film formation. In contrast, bionanocomposites supplemented with amyloid fibrils derived from the short I_{10} peptide did not exhibit any significant changes in their mechanical properties (**Figures 2 and S6**). For full length IAPP, CNF films supplemented with 0.4 wt % and 2 wt % of assembled peptide did not exhibit any significant change in mechanical properties (**Figure S6**), whereas the addition of 10 mg IAPP fibrils, 4 wt %, improved significantly Young's modulus tensile stress, and strain energy. These data indicating that CsgA fibrils, in contrast to amyloid fibrils assembled with peptides, improve mechanical properties up to 7-fold are likely associated with the web-like and high intertwined morphology of curli fibrils, which confer high capacity to adhere to surfaces and mechanical resistance to bacterial biofilm. Similarly, it has been recently reported for CNMs, that the addition of proteinaceous amyloid fibrils derived from lysozyme led to a negligible, or slight, improvement of mechanical properties of the composites, further indicating the unique properties of CsgA fibrils as reinforcing agent[20, 22, 23]. Overall, these results revealed that low amounts, *i.e.* 0.4 wt%, or 3.49 $mg.cm^{-3}$, of curli fibrils significantly increased the mechanical properties of CNF bionanocomposites. This observation correlates with a recent study reporting that the incorporation of CsgA fibrils within alginate nanocomposite hydrogels results in improved Young's modulus/stiffness (up to 4-fold), without altering the alginate support film's appearance and chemical properties[13].

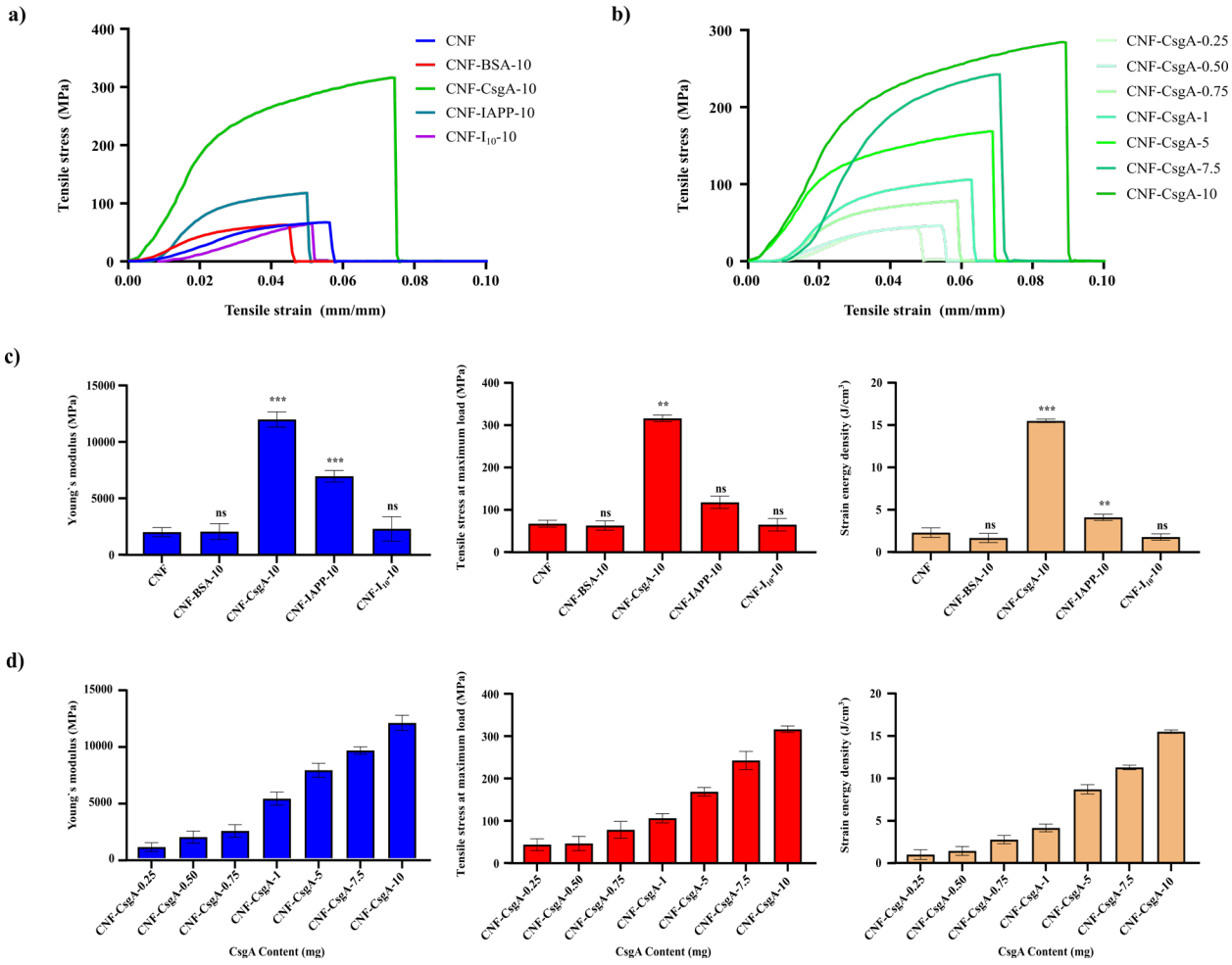

Figure 2. Mechanical characterization of CNF films supplemented with proteins. Typical stress-strain curves (**a, b**) and derived mechanical properties (**c, d**) (Young's modulus/stiffness, tensile stress at maximum load/strength, strain energy density/toughness) of CNF films where the proteins were incorporated into CNF matrix as pre-assembled amyloid fibrils. Effects of different proteins nanostructures (**a, c**) and (**b, d**) of different amount of CsgA loaded into the CNF films.

Supplementing CNF Films with CsgA Fibrils Increases Surface Hydrophobicity and Thermal Stability. Nanocellulose-based materials show considerable hydrophilicity, limiting their potential when water-repellent properties are required[44]. Methods employed to enhance the hydrophobicity of CNF include esterification, carbanilation, and silylation that required chemicals, hazardous organic solvents and specialized equipment, which result in high processing costs and

raise environmental concerns[45]. The addition of hydrophobic proteinaceous nanostructures such as curli fibrils could be a sustainable strategy to increase the hydrophobicity of CNFs. Accordingly, we investigated how supplementing CNF films with CsgA fibrils affects the hydrophobicity of resulting bionanocomposites by evaluating surface wettability through water contact angle measurement. A low contact angle (< 90°) with water indicates hygroscopic and hydrophilic film properties, whereas hydrophobic surfaces have contact angle values over 90°[46]. CNFs are oxidized cellulose and consist of carboxylated β-D-glucopyranose units with hydroxyl and carboxyl groups, accounting for its hydrophilicity. As expected, CNF exhibited a typical high-water affinity associated with a contact angle of 58.99 ° (**Figure 3a**), in agreement with previous studies suggesting that CNF-based films are vulnerable to water[25, 47]. The addition of 4 wt % CsgA fibrils to CNFs significantly decreased the hydrophilic character of the film surface, as observed with a water contact angle of 116.32°. A slightly significant increment (~12%) in the water contact angle for the film supplemented with 4 wt % BSA was present in comparison to CNF film (**Figure 2a**). This effect could be associated with potential hydrogen bonding between the CNF and BSA that modify the surface porosity, and thus decrease the surface free energy, which slightly increases the hydrophobicity[46, 48]. Nonetheless, the water contact angle measured for the CNF-CsgA film was significantly higher than that measured for CNF films supplemented with BSA. In this view, CsgA assemblies were more hydrophobic than soluble BSA, as observed by measuring the fluorescence of ANS, whose fluorescence quantum yield increases upon binding to hydrophobic patches (**Figure S8)**.

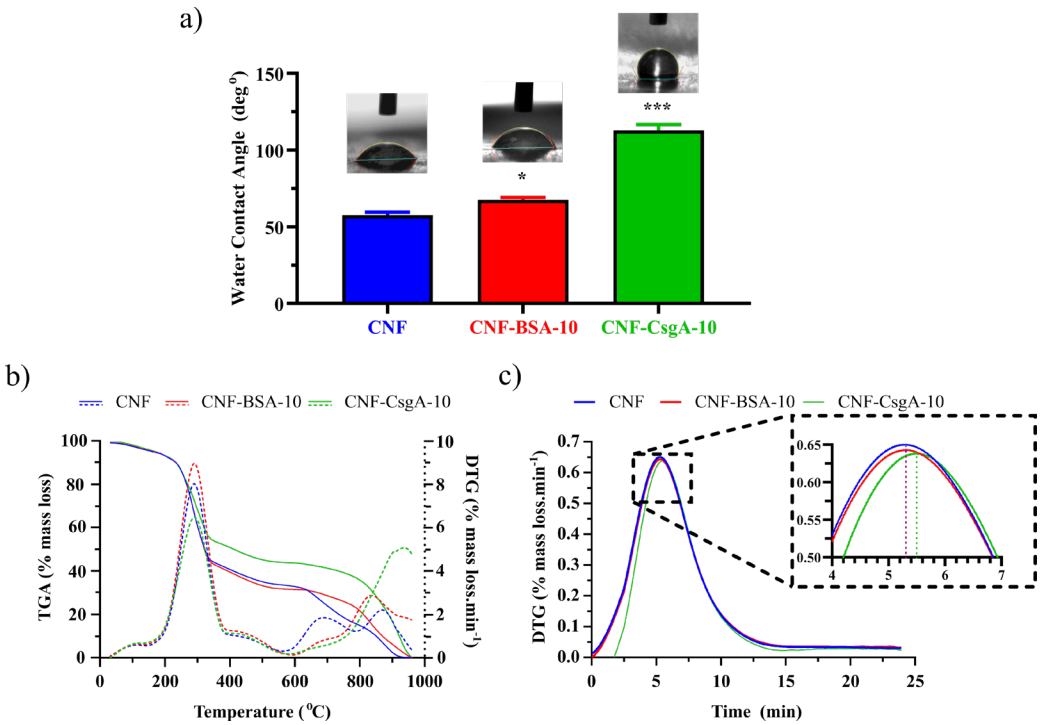

Figure 3. Physical properties of CNF films supplemented with CsgA fibrils. (**a**) Water contact angle characterization of CNF, CNF-BSA-10 and CNF-CsgA-10 films. (**b**) Thermal stability experiments by TGA and DTG from 30 °C to 960 °C enclosing the thermal decomposition process of CNF, CNF-BSA-10 and CNF-CsgA-10 films. (**c**) Dehydration profiles of the films are shown through the DTG of a 110 °C isothermal experiment. Both experiments were conducted under normal pressure and in an inert atmosphere under Ar (g). Inset in (**c**) highlights the peak maximum of CNF-CsgA-10 film at 5.5 min, while those of CNF and CNF-BSA-10 were at 5.3 min.

Next, we evaluated the impact of supplementing CNF film with CsgA fibrils on the biocomposite thermal stability. Thermogravimetric analyses from a near ambient temperature of 30 °C to a high heat zone of 960 °C produced TGA curves and derivative thermal gravimetry (DTG) plots to identify the mass loss proportions at peak temperatures (**Figure 3b**). The addition of CsgA had significant effect on the thermal decomposition process from 30 °C to 250 °C, where dehydration is between 30 °C to 110 °C and the pyrolysis onset is at 156°C[49, 50]. From 250 °C to 575 °C, the pyrolysis of CNF (~8%) and CNF-BSA (~9%) films led to a larger mass loss compared to CNF-CsgA (~6.8%). At the end of pyrolysis, *i.e.* between 575 °C and 960 °C, the CNF-CsgA films showed a single intense peak at around 940 °C. These observations indicated that the CNF-

CsgA film experienced a lower gradual mass loss compared to CNF and CNF-BSA films, suggestive of improved resistance to heat, as previously reported [51]. On the isothermal DTG at 110 ºC for 20 minutes, the curves peaked at 5 - 6 min (**Figure 3c**). The CNF and CNF-BSA-10 film dehydration profiles were completely superimposable, but that of the CNF-CsgA-10 film was not. The CNF-CsgA-10 film percent weight loss maximum was delayed to 5.5 min (**Figure 3 c-inset**).

Organization of Curli Fibrils within CNF Films. FITR spectroscopy was first used to probe the incorporation of the protein constituents within CNF films. ATR-FTIR spectra of unmodified CNF film exhibited several characteristic bands attributed to oxidized cellulose macromolecules such as ~3300 cm^{-1}, ~2900 cm^{-1} and ~1025 cm^{-1} for stretching vibration of O-H, C-H, or -CH_2 and C-O of secondary alcohols, respectively[52, 53] (**Figure 4a**). The peak at ~1350 cm^{-1} corresponded to bending vibrations of C-H bonds of glucose rings[52, 54] while the peak at ~1615 cm^{-1} represented the carbonyl stretching, resulting from surface sodium carboxylate groups obtained after TEMPO oxidation[54]. CsgA and BSA alone exhibited distinguishable amide peaks at ~1650 cm^{-1} and ~1525 cm^{-1}, which were attributed to the amide I band (C=O) and amide II band (C-N), respectively. The appearance of both amide peaks in the CNF-CsgA films confirmed the incorporation of the proteinaceous constituent within the CNF matrix. Intriguingly, peaks corresponding to the amide group were poorly distinguishable by FTIR for the CNF-BSA films. To further confirm the presence of proteins within the film and to understand why the amide bands were not observed by FTIR for the CNF-BSA sample, we conducted elemental analysis of the first 10 to 20 nm depth of the surface by XPS. Apart from variable salt content (Na^+, Cl^-) and a difference in the nitrogen signal, the acquired surveys were similar (**Figure 4b**). High-resolution

spectra of C_{1s}, N_{1s} and O_{1s} further confirmed protein inclusion in both protein-supplemented films, although weaker signals were observed for CNF-BSA film (**Figure S9** and **Table S3**). The CNF film C_{1s} peak was specific for the bond signals found in CNF. The C_{1s} signals from CNF-BSA-10 and CNF-CsgA-10 differed with the addition of two bonds, C-N at 286.0 eV and O=C-N at 288.2 eV ascribed to the added protein. These variability in the intensities recorded likely indicate the surface localization of CsgA versus the probably deeper, or more uniform, distribution of BSA. Additionally, for the O_{1s} signal, the intensification of the O-C=N at 531.5 eV signal for CNF-CsgA-10 was noteworthy, compared to CNF-BSA-10, further suggesting an increase of surface content of CsgA protein on CNF-CsgA-10, compared to BSA on the CNF-BSA-10 film.

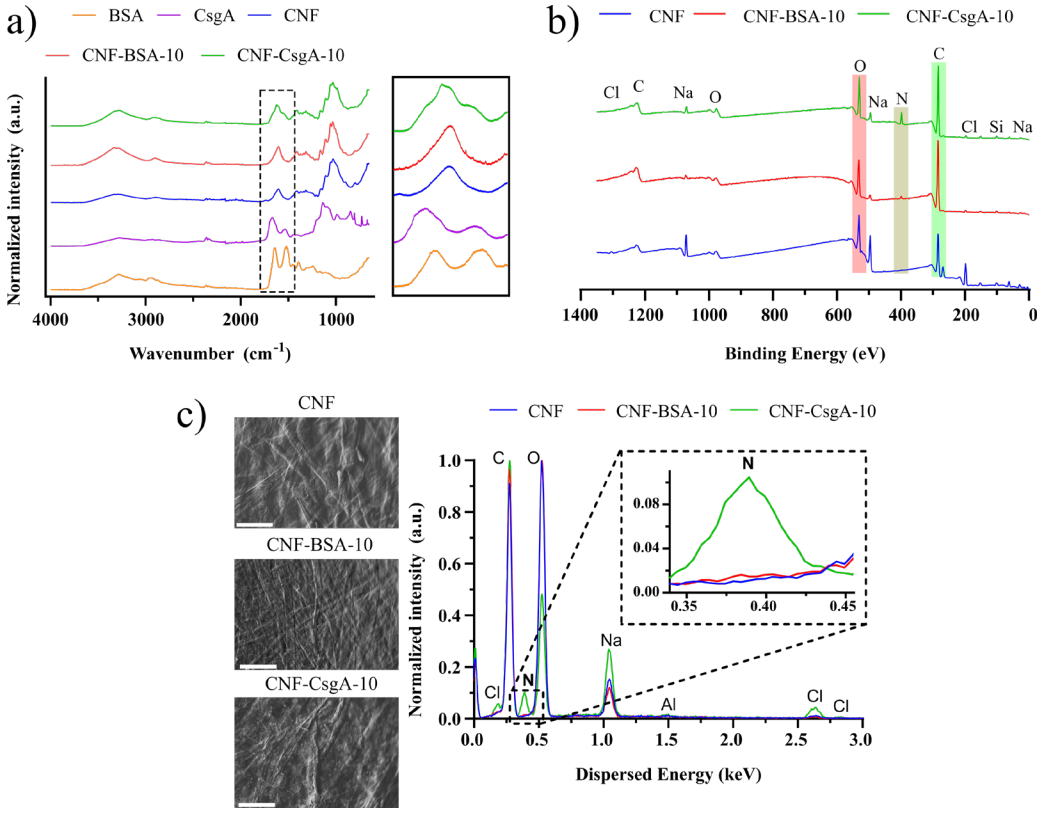

Figure 4. Attenuated total reflectance Fourier-transform infrared spectroscopy spectra of proteins and CNF bionanocomposites (**a**). XPS survey of CNF, CNF-BSA-10, and CNF-CsgA-10 films. Oxygen (O), nitrogen (N) and carbon (C) signals are highlighted in red, dark-yellow and green, respectively (**b**). SEM images and EDXS spectra of CNF, CNF-BSA-10 and CNF-CsgA-10 film surfaces (**c**). The scale bars are 100 µm. Inset spectra in (**a**) is a magnification of the amide I and

II regions of the FTIR spectrum and in (**c**) is a magnification of the nitrogen (N) element detected signal.

Continuing our investigation regarding the protein localization within the CNF films, EDXS analysis was conducted on representative areas of the films (**Figure 4c**). EDXS is an elemental characterization approach that detect elemental nitrogen in films. Knowing that the depth of analysis by EDXS is 500 nm - 2 μm, we could evaluate whether BSA was buried into the film depths and if CsgA was preferentially located on the surface. The acquired spectra showed that the nitrogen content was similar for both CNF and CNF-BSA (**Figure 4c**). In contrast, the N signal from CNF-CsgA film was ~9-fold higher than from the control films. Such results not only confirm XPS analysis, but further suggest that CsgA is detectable up to 2 μm from the surface. Besides, the detection of nitrogen in XPS and the absence of detection of nitrogen in the EDXS spectrum of CNF-BSA is due to the comparably higher sensitivity of the XPS instrument[55]. When 10 times more mass loading of BSA was incorporated in the CNF film (*i.e.* 40 wt %), the signals were detected by both XPS and EDXS (**Figure S10**). This suggests that BSA was below the detection limit of EDXS in the CNF-BSA-10 film. BSA's solubility and mobility within CNF film led to a homogenous blend throughout the ~50 μm thickness, thus diluting its signal within the bulk. FTIR and EDXS are classified as bulk characterization techniques and are therefore indifferent to the amide resonant bands and nitrogen element emitted X-rays of BSA traces in the film[56]. On the other hand, XPS reports exclusively on the surface elemental composition and is more sensitive to subtle BSA concentrations[57]. CsgA is a hydrophobic molecule (**Figure S8**), supporting its surface distribution on the hydrophilic CNF film (**Figure S11**). Surface assembled CsgA likely contributes to the adhesive forces of the CNF film, making the film increasingly tensile when compared to those made with BSA. This model correlates well the dehydration results presented above.

Although the CNF film is hydrophilic favoring water displacement, when covered by hydrophobic sheets of CsgA, water vapor found itself obstructed and effectively trapped in the CNF film matrix, sandwiched between two repelling layers of CsgA at each facet of the film.

CsgA Fibrils Modulate Surface Topology of CNF Films. The CNF and CNF-protein films were further characterized by AFM to examine their surface morphology. CNFs observed on the film were individual fibers randomly oriented with variable lengths (**Figure 5a**). Their thickness systematically ranged between 12 to 27 nm and their heights measured between 3 to 7 nm. On a 1 μm^2 scan frame, the roughness was evaluated at 6.3 nm. The topography of the CNF-BSA film did not present any visible differences compared to CNF alone, and the fiber-like morphology was retained (**Figure 5b**). In sharp contrast, it was apparent that CsgA partially covered and filled the gaps between the CNFs (**Figure 5c**). Surface morphology showed brushstroke patterns irregularly oriented in all three axes. Therefore, the calculated roughness increased to 7.8 nm and the maximum recorded height increased to 65 nm. These observations further support the preferential location on the CNF film surface.

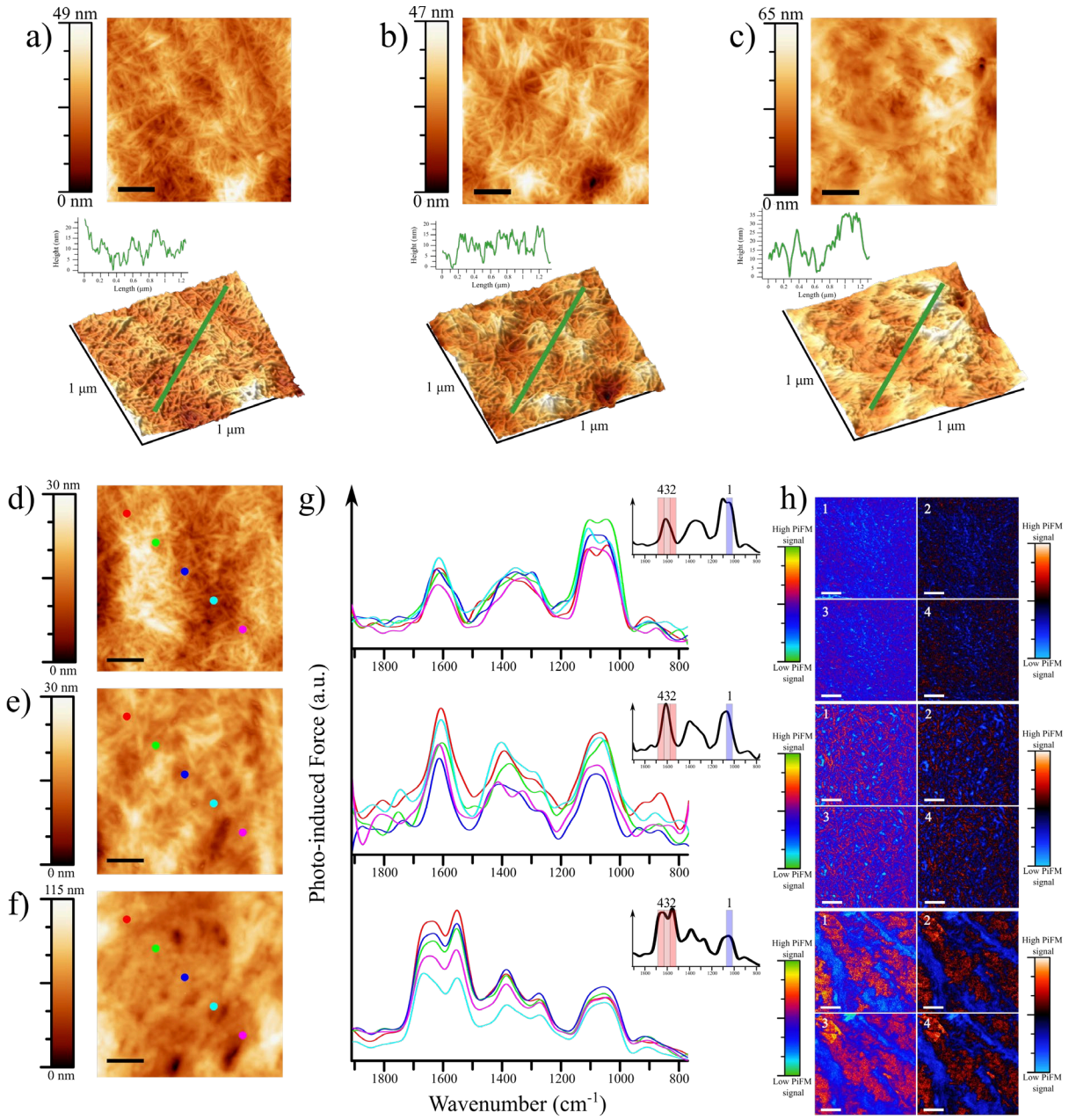

Figure 5. AFM 2D and 3D representations of (**a**) CNF, (**b**) CNF-BSA-10 and (**c**) CNF-CsgA-10 films. The scale bars on the 2D topography images are 200 nm and the insets above the 3D representations are the height profiles measured by the line traces. (**d**) CNF, (**e**) CNF-BSA-10 and (**f**) CNF-CsgA-10 film PiFM topography 2D images. (**g**) Corresponding point PiF-IR spectra and averaged PiF-IR spectra in the inset. (**h**) Chemical contrast images scanned at the wavelengths highlighted in blue and in shades of red on the average spectra, annotated by 1, 2, 3 and 4. The scale bars on the PiFM topography and chemical contrast images are 200 nm.

Next, high-resolution surface chemical characterization was performed to gain further information on the organization of the bionanocomposites (**Figure S12**). PiFM can chemically

identify topographical features, and therefore resolve the constituents of the bionanocomposites. The spatial resolution of each PiFM spectrum is known to be < 10 nm. In sideband mode, its chemical sensitivity extends up to 10-20 nm below the sample surface[58]. This implies that PiFM returns the same information as FTIR, but at a scale, one billion times more precisely confined on the sample surface. Spectra recorded in the mid-infrared between 770-1910 cm^{-1} on the topography scans (**Figures 5 d-f**) of CNF, CNF-BSA-10 and CNF-CsgA-10 had distinct peaks (**Figure 5g**). The substrate signals ascribed to the CNF were strong peaks within 1000-1175 cm^{-1} arising from either C-O stretching, C-C stretching, C-OH bending, or C-O-C pyranose ring stretching vibrations[49, 50]. Some less intense signals were seen at 1250-1500 cm^{-1}, caused by CH_2 scissoring, C-H bending, CH_2 wagging, and at 1550-1675 cm^{-1} from O-H bending of adsorbed water or -C=O stretching of the surface carboxylic groups[50]. As with the FTIR spectrum (**Figure 4a**), CNF-BSA-10 showed a intense peak at aorund 1550-1675 cm^{-1} due to amide absorption in the protein backbone structure[59], indicating that BSA was present in the films. On CNF-CsgA-10, the high wavenumber region was intensified compared to the control films. The CNF-CsgA-10 film showed a broader peak at 1550-1675 cm^{-1}, with two maxima, characteristic of amide II at ~1520-1550 cm^{-1} and amide I at ~1637 cm^{-1}. Raw average spectra peak assignment also confirmed protein identity[60] (**Figure S12a**). However, the CNF-CsgA-10 spectra displayed a more intense protein signal (1550-1675 cm^{-1}) than those of CNF-BSA-10, suggesting that more CsgA was localized on the surface of the film. Chemical contrast images at a low wavenumber region (depicted as blue) and at several high region wavenumbers (depicted as red) illustrated the distribution of the protein on the films' surface (**Figure 5h**). The CNF maps had no differences in the PiFM signal, as intensity distributions at every scan (low and high wavenumbers) were identical. For CNF-BSA-10, intense spots of BSA signals contrasted with the CNF, suggesting

that BSA was homogeneously distributed within the film. This is supported by the XPS and EDXS findings that BSA was well distributed in the film volume, making its concentration per unit volume dilute. Similarly, when adding 10 times more BSA in the bionanocomposite, *i.e.* CNF-BSA-100, BSA retained the uniform and homogeneous distribution (**Figure S12b**). For CNF-CsgA-10, large and gathered domains of CsgA occupied at least half of the scanned surface. The topological correspondence of CNF-CsgA-10 and CNF-BSA-10 with their PiFM maps show that the CNF fibrils were covered by CsgA in the former, while they were more spaced out in the latter. This suggests that CsgA first filled between the individual CNF fibrils, forming anchors for additional CsgA fibers, leading to vast surface domains. On the contrary, BSA protein filed between or passed through the CNF fibrils to migrate toward the film's core and disperse during film drying. Point-spectral acquisition atop a high PiFM intensity zone in comparison to a low PiFM intensity zone confirmed that the peaks at higher wavenumbers were accurate markers of CsgA (**Figure S12c**). In the PiFM-intense regions, the protein signals contributed ~70% in intensity compared to CNF in low-intense regions.

CONCLUSIONS

In conclusion, the present study underlines the use of amyloids derived from bacterial biofilms to increase the mechanical and physical properties of CNF nanoassemblies, expanding the possibilities for their use in applications where CNFs are convenient but need additional stiffness, strength, toughness, and/or hydrophobicity. Inspired by previous work showing an increase of CsgA-alginate hydrogel physical properties, we prepared and evaluated the CNF analogous bionanocomposite supplemented with nanofilaments prepared from recombinant CsgA. In contrast to fibrils assembled from synthetic peptides, addition of CsgA fibrils into CNF film improved the mechanical properties up to 7-fold, with only 4% wt of protein. The observed mechanical enhancement with CsgA fibrils was substantially more than those previously reported using other amyloid fibrils derived from naturally non-aggregating proteins. CsgA-CNF bionanocomposites also exhibited interesting wettability and thermal tolerance. Bulk spectroscopic characterization of CNF films using FTIR, XPS and EDXS confirmed CsgA amyloid embodiment in the CNF films. AFM and PiFM locally, optically, and chemically described surface amyloid-CNF morphology in high resolution. As is the case for other composites[13, 61], it is likely that favorable interactions between CsgA fibrils and the CNF matrix, combined with the high rigidity of bacterial amyloids, led to the observed increase in mechanical (stiffness, strength and toughness) and functional characteristics (hydrophobicity and thermal tolerance) of resulting bionanocomposites. Taken together, this study supports the development of novel bionanocomposites from interconnecting necessary properties of both amyloid fibrils derived from bacterial biofilm and cellulosic materials for future miscellaneous applications.

ASSOCIATED CONTENT

Supporting information

The Supporting Information is available free of charge at: https://pubs.acs.org/doi/

Schematic representation of the preparation of bionanocomposites, TEM images of CNFs, SDS-PAGE analysis of the CsgA, HPLC and mass spectrometry analysis of IAPP and I_{10} synthetic peptides, mechanical characterization of CNF films supplemented with non-assembled proteins, hydrophobicity of BSA and CsgA by ANS fluorescence, XPS high-resolution spectra, quantitative elemental composition analysis, XPS and EDXS analysis of CNF-BSA-100, hypothesized schematic 3D sections of the CNFs, detailed PiFM analysis.

Notes

The authors declare no competing financial interest.

ACKNOWLEDGMENTS

This reserach was supported by funding from the Natural Sciences and Engineering Research Council of Canada (NSERC), grants RGPIN-2018-06209 (S.B.), RGPIN-2021-02861 (E.L.), and RGPIN-2016-06532 (D.A.).

REFERENCES

(1) Mousa, M. H.; Dong, Y.; Davies, I. J. Recent advances in bionanocomposites: Preparation, properties, and applications. *International Journal of Polymeric Materials and Polymeric Biomaterials* **2016**, *65* (5), 225-254. DOI: 10.1080/00914037.2015.1103240.
(2) Bealer, E. J.; Onissema-Karimu, S.; Rivera-Galletti, A.; Francis, M.; Wilkowski, J.; Salas-de la Cruz, D.; Hu, X. Protein–polysaccharide composite materials: Fabrication and applications. *Polymers* **2020**, *12* (2), 464.
(3) Zottig, X.; Cote-Cyr, M.; Arpin, D.; Archambault, D.; Bourgault, S. Protein Supramolecular Structures: From Self-Assembly to Nanovaccine Design. *Nanomaterials (Basel)* **2020**, *10* (5), Review. DOI: 10.3390/nano10051008.
(4) Gazit, E. Controlling molecular self-assembly: from amyloid oligomerization and therapy to novel biomaterials and technological applications in nanomedicine. *Nanomedicine (Lond)* **2014**, *9* (16), 2433-2436, Editorial. DOI: 10.2217/nnm.14.173.
(5) Chiti, F.; Dobson, C. M. Protein Misfolding, Amyloid Formation, and Human Disease: A Summary of Progress Over the Last Decade. *Annual review of biochemistry* **2017**, *86*, 27-68, Historical Article

Review. DOI: 10.1146/annurev-biochem-061516-045115.
(6) Otzen, D.; Riek, R. Functional Amyloids. *Cold Spring Harb Perspect Biol* **2019**, *11* (12), Review. DOI: 10.1101/cshperspect.a033860.
(7) Chiti, F.; Dobson, C. M. Protein misfolding, amyloid formation, and human disease: a summary of progress over the last decade. *Annu. Rev. Biochem* **2017**, *86* (1), 27-68.
(8) Schleeger, M.; Deckert-Gaudig, T.; Deckert, V.; Velikov, K. P.; Koenderink, G.; Bonn, M. Amyloids: from molecular structure to mechanical properties. *Polymer* **2013**, *54* (10), 2473-2488.
(9) Adamcik, J.; Lara, C.; Usov, I.; Jeong, J. S.; Ruggeri, F. S.; Dietler, G.; Lashuel, H. A.; Hamley, I. W.; Mezzenga, R. Measurement of intrinsic properties of amyloid fibrils by the peak force QNM method. *Nanoscale* **2012**, *4* (15), 4426-4429.
(10) Fitzpatrick, A. W.; Debelouchina, G. T.; Bayro, M. J.; Clare, D. K.; Caporini, M. A.; Bajaj, V. S.; Jaroniec, C. P.; Wang, L.; Ladizhansky, V.; Müller, S. A. Atomic structure and hierarchical assembly of a cross-β amyloid fibril. *Proceedings of the National Academy of Sciences* **2013**, *110* (14), 5468-5473.
(11) Dorval Courchesne, N. m.-M.; Duraj-Thatte, A.; Tay, P. K. R.; Nguyen, P. Q.; Joshi, N. S. Scalable production of genetically engineered nanofibrous macroscopic materials via filtration. *ACS Biomaterials Science & Engineering* **2017**, *3* (5), 733-741.
(12) Duraj-Thatte, A. M.; Manjula-Basavanna, A.; Courchesne, N.-M. D.; Cannici, G. I.; Sánchez-Ferrer, A.; Frank, B. P.; van't Hag, L.; Cotts, S. K.; Fairbrother, D. H.; Mezzenga, R. Water-processable, biodegradable and coatable aquaplastic from engineered biofilms. *Nature chemical biology* **2021**, *17* (6), 732-738.
(13) Axpe, E.; Duraj-Thatte, A.; Chang, Y.; Kaimaki, D.-M.; Sanchez-Sanchez, A.; Caliskan, H. B.; Dorval Courchesne, N. m.-M.; Joshi, N. S. Fabrication of amyloid curli fibers–alginate nanocomposite hydrogels with enhanced stiffness. *ACS Biomaterials Science & Engineering* **2018**, *4* (6), 2100-2105.
(14) Moon, R. J.; Schueneman, G. T.; Simonsen, J. Overview of cellulose nanomaterials, their capabilities and applications. *Jom* **2016**, *68* (9), 2383-2394.
(15) de Assis, C. A.; Houtman, C.; Phillips, R.; Bilek, E.; Rojas, O. J.; Pal, L.; Peresin, M. S.; Jameel, H.; Gonzalez, R. Conversion economics of forest biomaterials: risk and financial analysis of CNC manufacturing. *Biofuels, Bioproducts and Biorefining* **2017**, *11* (4), 682-700. de Assis, C. A.; Iglesias, M. C.; Bilodeau, M.; Johnson, D.; Phillips, R.; Peresin, M. S.; Bilek, E.; Rojas, O. J.; Venditti, R.; Gonzalez, R. Cellulose micro-and nanofibrils (CMNF) manufacturing-financial and risk assessment. *Biofuels, Bioproducts and Biorefining* **2018**, *12* (2), 251-264. Li, M.-C.; Wu, Q.; Song, K.; Qing, Y.; Wu, Y. Cellulose nanoparticles as modifiers for rheology and fluid loss in bentonite water-based fluids. *ACS applied materials & interfaces* **2015**, *7* (8), 5006-5016. Nasseri, R.; Deutschman, C.; Han, L.; Pope, M.; Tam, K.

Cellulose nanocrystals in smart and stimuli-responsive materials: a review. *Materials Today Advances* **2020**, *5*, 100055.
(16) De France, K. J.; Hoare, T.; Cranston, E. D. Review of hydrogels and aerogels containing nanocellulose. *Chemistry of Materials* **2017**, *29* (11), 4609-4631. Thomas, B.; Raj, M. C.; Joy, J.; Moores, A.; Drisko, G. L.; Sanchez, C. Nanocellulose, a versatile green platform: from biosources to materials and their applications. *Chemical reviews* **2018**, *118* (24), 11575-11625.
(17) Iwamoto, S.; Kai, W.; Isogai, A.; Iwata, T. Elastic Modulus of Single Cellulose Microfibrils from Tunicate Measured by Atomic Force Microscopy. *Biomacromolecules* **2009**, *10* (9), 2571-2576. DOI: 10.1021/bm900520n. Zhai, L.; Kim, H. C.; Kim, J. W.; Kang, J.; Kim, J. Elastic moduli of cellulose nanofibers isolated from various cellulose resources by using aqueous counter collision. *Cellulose* **2018**, *25* (7), 4261-4268. DOI: 10.1007/s10570-018-1836-x.
(18) Alexopoulos, P.; O'sullivan, T. Mechanical properties of thin films. *Annual review of materials science* **1990**, *20* (1), 391-420.
(19) Mokhena, T. C.; Sadiku, E. R.; Mochane, M. J.; Ray, S. S.; John, M. J.; Mtibe, A. Mechanical properties of cellulose nanofibril papers and their bionanocomposites: A review. *Carbohydrate Polymers* **2021**, *273*, 118507.
(20) De France, K. J.; Kummer, N.; Ren, Q.; Campioni, S.; Nyström, G. Assembly of Cellulose Nanocrystal–Lysozyme Composite Films with Varied Lysozyme Morphology. *Biomacromolecules* **2020**, *21* (12), 5139-5147.
(21) Chuang, C. T.; Chao, C. K.; Chang, R. C.; Chu, K. Y. Effects of internal stresses on the mechanical properties of deposition thin films. *Journal of Materials Processing Technology* **2008**, *201* (1), 770-774. DOI: https://doi.org/10.1016/j.jmatprotec.2007.11.258. Gojny, F. H.; Wichmann, M. H. G.; Fiedler, B.; Schulte, K. Influence of different carbon nanotubes on the mechanical properties of epoxy matrix composites – A comparative study. *Composites Science and Technology* **2005**, *65* (15), 2300-2313. DOI: https://doi.org/10.1016/j.compscitech.2005.04.021. Zhao, J.; Zhang, X.; Di, J.; Xu, G.; Yang, X.; Liu, X.; Yong, Z.; Chen, M.; Li, Q. Double-Peak Mechanical Properties of Carbon-Nanotube Fibers. *Small* **2010**, *6* (22), 2612-2617, https://doi.org/10.1002/smll.201001120. DOI: https://doi.org/10.1002/smll.201001120 (acccessed 2023/03/27). Jeon, J. G.; Kim, H. C.; Palem, R. R.; Kim, J.; Kang, T. J. Cross-linking of cellulose nanofiber films with glutaraldehyde for improved mechanical properties. *Materials Letters* **2019**, *250*, 99-102. DOI: https://doi.org/10.1016/j.matlet.2019.05.002. Kim, H. C.; Kim, D.; Lee, J. Y.; Zhai, L.; Kim, J. Effect of Wet Spinning and Stretching to Enhance Mechanical Properties of Cellulose Nanofiber Filament. *International Journal of Precision Engineering and Manufacturing-Green Technology* **2019**, *6* (3), 567-575. DOI: 10.1007/s40684-019-00070-z. Orelma, H.; Korpela, A.; Kunnari, V.; Harlin, A.; Suurnäkki, A. Improving the mechanical properties of CNF films by NMMO partial dissolution with hot calender activation. *Cellulose* **2017**, *24* (4), 1691-1704. DOI: 10.1007/s10570-017-1229-6.
(22) Atoufi, Z.; Cinar Ciftci, G.; Reid, M. S.; Larsson, P. A.; Wågberg, L. Green Ambient-Dried Aerogels with a Facile pH-Tunable Surface Charge for Adsorption of Cationic and Anionic Contaminants with High Selectivity. *Biomacromolecules* **2022**, *23* (11), 4934-4947. Severini, L.; De France, K. J.; Sivaraman, D.; Kummer, N.; Nystrom, G. Biohybrid Nanocellulose-Lysozyme Amyloid Aerogels via Electrostatic Complexation. *ACS Omega* **2022**, *7* (1), 578-586. DOI: 10.1021/acsomega.1c05069 From NLM PubMed-not-MEDLINE. Kummer, N.; Giacomin, C. E.; Fischer, P.; Campioni, S.; Nystrom, G. Amyloid fibril-nanocellulose interactions and self-assembly. *J Colloid Interface Sci* **2023**, *641*, 338-347. DOI: 10.1016/j.jcis.2023.03.002 From NLM Medline. De France, K. J.; Kummer, N.; Campioni, S.; Nystrom, G. Phase Behavior, Self-Assembly, and Adhesive Potential of Cellulose Nanocrystal-Bovine Serum Albumin Amyloid Composites. *ACS Appl Mater Interfaces* **2023**, *15* (1), 1958-1968. DOI: 10.1021/acsami.2c14406 From NLM Medline.

(23) Silva, N. H.; Figueira, P.; Fabre, E.; Pinto, R. J.; Pereira, M. E.; Silvestre, A. J.; Marrucho, I. M.; Vilela, C.; Freire, C. S. Dual nanofibrillar-based bio-sorbent films composed of nanocellulose and lysozyme nanofibrils for mercury removal from spring waters. *Carbohydrate polymers* **2020**, *238*, 116210.
(24) Evans, M. L.; Chapman, M. R. Curli biogenesis: order out of disorder. *Biochimica et Biophysica Acta (BBA)-Molecular Cell Research* **2014**, *1843* (8), 1551-1558.
(25) Bideau, B.; Bras, J.; Saini, S.; Daneault, C.; Loranger, E. Mechanical and antibacterial properties of a nanocellulose-polypyrrole multilayer composite. *Materials Science and Engineering: C* **2016**, *69*, 977-984.
(26) Zottig, X.; Al-Halifa, S.; Babych, M.; Quittot, N.; Archambault, D.; Bourgault, S. Guiding the morphology of amyloid assemblies by electrostatic capping: from polymorphic twisted fibrils to uniform nanorods. *Small* **2019**, *15* (33), 1901806.
(27) Lamontagne, F.; Arpin, D.; Cote-Cyr, M.; Khatri, V.; St-Louis, P.; Gauthier, L.; Archambault, D.; Bourgault, S. Engineered Curli Nanofilaments as a Self-Adjuvanted Antigen Delivery Platform. *Adv Healthc Mater* **2023**, e2300224. DOI: 10.1002/adhm.202300224 From NLM Publisher.
(28) Godin, E.; Nguyen, P. T.; Zottig, X.; Bourgault, S. Identification of a hinge residue controlling islet amyloid polypeptide self-assembly and cytotoxicity. *J Biol Chem* **2019**, *294* (21), 8452-8463, Research Support, Non-U.S. Gov't. DOI: 10.1074/jbc.RA118.006454.
(29) Zottig, X.; Al-Halifa, S.; Cote-Cyr, M.; Calzas, C.; Le Goffic, R.; Chevalier, C.; Archambault, D.; Bourgault, S. Self-assembled peptide nanorod vaccine confers protection against influenza A virus. *Biomaterials* **2021**, *269*, 120672. DOI: 10.1016/j.biomaterials.2021.120672.
(30) Maury, C.; Crispino, F.; Loranger, É. Preliminary study of laminated glass with nanocellulose and poly (vinyl butyral) for safety glazing. *BioResources* **2019**, *14* (2), 4157-4170. Loranger, E.; Piché, A.-O.; Daneault, C. Influence of high shear dispersion on the production of cellulose nanofibers by ultrasound-assisted TEMPO-oxidation of kraft pulp. *Nanomaterials* **2012**, *2* (3), 286-297.
(31) Lassoued, M.; Crispino, F.; Loranger, E. Design and synthesis of transparent and flexible nanofibrillated cellulose films to replace petroleum-based polymers. *Carbohydrate Polymers* **2021**, *254*, 117411.
(32) Varasteh, R.; Hashemi, M.; Jaafari, m. r.; Moghadassi, M. Formulation of Anti-Rh (D) immunoglobulin preparation. *Iranian Journal of Basic Medical Science* **2004**, *7*.
(33) Horcas, I.; Fernández, R.; Gomez-Rodriguez, J.; Colchero, J.; Gómez-Herrero, J.; Baro, A. WSXM: A software for scanning probe microscopy and a tool for nanotechnology. *Review of scientific instruments* **2007**, *78* (1), 013705.
(34) Barnhart, M. M.; Chapman, M. R. Curli biogenesis and function. *Annual review of microbiology* **2006**, *60*, 131. McCrate, O. A.; Zhou, X.; Reichhardt, C.; Cegelski, L. Sum of the parts: composition and architecture of the bacterial extracellular matrix. *Journal of molecular biology* **2013**, *425* (22), 4286-4294.
(35) Pawar, D.; Rossman, M.; Chen, J. Role of curli fimbriae in mediating the cells of enterohaemorrhagic Escherichia coli to attach to abiotic surfaces. *Journal of applied microbiology* **2005**, *99* (2), 418-425.
(36) Wang, X.; Hammer, N. D.; Chapman, M. R. The molecular basis of functional bacterial amyloid polymerization and nucleation. *Journal of Biological Chemistry* **2008**, *283* (31), 21530-21539.
(37) Nguyen, P. T.; Zottig, X.; Sebastiao, M.; Arnold, A. A.; Marcotte, I.; Bourgault, S. Identification of transmissible proteotoxic oligomer-like fibrils that expand conformational diversity of amyloid assemblies. *Communications Biology* **2021**, *4* (1), 1-14.
(38) Nguyen, P. T.; Zottig, X.; Sebastiao, M.; Bourgault, S. Role of site-specific asparagine deamidation in islet amyloid polypeptide amyloidogenesis: key contributions of residues 14 and 21. *Biochemistry* **2017**, *56* (29), 3808-3817.
(39) Madine, J.; Jack, E.; Stockley, P. G.; Radford, S. E.; Serpell, L. C.; Middleton, D. A. Structural insights into the polymorphism of amyloid-like fibrils formed by region 20− 29 of amylin revealed by solid-state

NMR and X-ray fiber diffraction. *Journal of the American Chemical Society* **2008**, *130* (45), 14990-15001. Westermark, P.; Engström, U.; Johnson, K. H.; Westermark, G. T.; Betsholtz, C. Islet amyloid polypeptide: pinpointing amino acid residues linked to amyloid fibril formation. *Proceedings of the National Academy of Sciences* **1990**, *87* (13), 5036-5040.
(40) Sebastiao, M.; Quittot, N.; Bourgault, S. Thioflavin T fluorescence to analyse amyloid formation kinetics: Measurement frequency as a factor explaining irreproducibility. *Analytical biochemistry* **2017**, *532*, 83-86.
(41) Dueholm, M. S.; Nielsen, S. B.; Hein, K. L.; Nissen, P.; Chapman, M.; Christiansen, G.; Nielsen, P. H.; Otzen, D. E. Fibrillation of the major curli subunit CsgA under a wide range of conditions implies a robust design of aggregation. *Biochemistry* **2011**, *50* (39), 8281-8290.
(42) Nair, S. S.; Zhu, J.; Deng, Y.; Ragauskas, A. J. Hydrogels prepared from cross-linked nanofibrillated cellulose. *ACS Sustainable Chemistry & Engineering* **2014**, *2* (4), 772-780. Khalil, H. A.; Davoudpour, Y.; Islam, M. N.; Mustapha, A.; Sudesh, K.; Dungani, R.; Jawaid, M. Production and modification of nanofibrillated cellulose using various mechanical processes: a review. *Carbohydrate polymers* **2014**, *99*, 649-665. Kafy, A.; Kim, H. C.; Zhai, L.; Kim, J. W.; Hai, L. V.; Kang, T. J.; kim, J. Cellulose long fibers fabricated from cellulose nanofibers and its strong and tough characteristics. *Scientific Reports* **2017**, *7* (1), 17683. DOI: 10.1038/s41598-017-17713-3. Van Hai, L.; Zhai, L.; Kim, H. C.; Kim, J. W.; Choi, E. S.; Kim, J. Cellulose nanofibers isolated by TEMPO-oxidation and aqueous counter collision methods. *Carbohydrate Polymers* **2018**, *191*, 65-70. DOI: https://doi.org/10.1016/j.carbpol.2018.03.008. Zeng, J.; Zeng, Z.; Cheng, Z.; Wang, Y.; Wang, X.; Wang, B.; Gao, W. Cellulose nanofibrils manufactured by various methods with application as paper strength additives. *Scientific Reports* **2021**, *11* (1), 11918. DOI: 10.1038/s41598-021-91420-y.
(43) Deepa, B.; Abraham, E.; Cordeiro, N.; Mozetic, M.; Mathew, A. P.; Oksman, K.; Faria, M.; Thomas, S.; Pothan, L. A. Utilization of various lignocellulosic biomass for the production of nanocellulose: a comparative study. *Cellulose* **2015**, *22* (2), 1075-1090. DOI: 10.1007/s10570-015-0554-x. Moon, R. J.; Martini, A.; Nairn, J.; Simonsen, J.; Youngblood, J. Cellulose nanomaterials review: structure, properties and nanocomposites. *Chemical Society Reviews* **2011**, *40* (7), 3941-3994, 10.1039/C0CS00108B. DOI: 10.1039/C0CS00108B. Sacui, I. A.; Nieuwendaal, R. C.; Burnett, D. J.; Stranick, S. J.; Jorfi, M.; Weder, C.; Foster, E. J.; Olsson, R. T.; Gilman, J. W. Comparison of the Properties of Cellulose Nanocrystals and Cellulose Nanofibrils Isolated from Bacteria, Tunicate, and Wood Processed Using Acid, Enzymatic, Mechanical, and Oxidative Methods. *ACS Applied Materials & Interfaces* **2014**, *6* (9), 6127-6138. DOI: 10.1021/am500359f.
(44) Habibi, Y. Key advances in the chemical modification of nanocelluloses. *Chemical Society Reviews* **2014**, *43* (5), 1519-1542. Liu, H.; Liu, D.; Yao, F.; Wu, Q. Fabrication and properties of transparent polymethylmethacrylate/cellulose nanocrystals composites. *Bioresource technology* **2010**, *101* (14), 5685-5692.
(45) Sato, A.; Kabusaki, D.; Okumura, H.; Nakatani, T.; Nakatsubo, F.; Yano, H. Surface modification of cellulose nanofibers with alkenyl succinic anhydride for high-density polyethylene reinforcement. *Composites Part A: Applied Science and Manufacturing* **2016**, *83*, 72-79. Wang, Y.; Wang, X.; Heim, L.-O.; Breitzke, H.; Buntkowsky, G.; Zhang, K. Superhydrophobic surfaces from surface-hydrophobized cellulose fibers with stearoyl groups. *Cellulose* **2015**, *22* (1), 289-299. Yuan, Z.; Wen, Y. Enhancement of hydrophobicity of nanofibrillated cellulose through grafting of alkyl ketene dimer. *Cellulose* **2018**, *25* (12), 6863-6871. Missoum, K.; Belgacem, M. N.; Bras, J. Nanofibrillated cellulose surface modification: a review. *Materials* **2013**, *6* (5), 1745-1766. Wu, C.-N.; Saito, T.; Yang, Q.; Fukuzumi, H.; Isogai, A. Increase in the water contact angle of composite film surfaces caused by the assembly of hydrophilic nanocellulose fibrils and nanoclay platelets. *ACS Applied Materials & Interfaces* **2014**, *6* (15), 12707-12712. Yan, Y.; Amer, H.; Rosenau, T.; Zollfrank, C.; Dörrstein, J.; Jobst, C.; Zimmermann, T.; Keckes, J.;

Veigel, S.; Gindl-Altmutter, W. Dry, hydrophobic microfibrillated cellulose powder obtained in a simple procedure using alkyl ketene dimer. *Cellulose* **2016**, *23* (2), 1189-1197.
(46) Lavrič, G.; Oberlintner, A.; Filipova, I.; Novak, U.; Likozar, B.; Vrabič-Brodnjak, U. Functional nanocellulose, alginate and chitosan nanocomposites designed as active film packaging materials. *Polymers* **2021**, *13* (15), 2523.
(47) Jung, Y. H.; Chang, T.-H.; Zhang, H.; Yao, C.; Zheng, Q.; Yang, V. W.; Mi, H.; Kim, M.; Cho, S. J.; Park, D.-W. High-performance green flexible electronics based on biodegradable cellulose nanofibril paper. *Nature communications* **2015**, *6* (1), 1-11.
(48) Hussain, M. M.; Chaudhary, M. A.; Razaq, A. Mechanism of saline deposition and surface flashover on high-voltage insulators near shoreline: Mathematical models and experimental validations. *Energies* **2019**, *12* (19), 3685.
(49) V H, S.; Varghese, T. O.; Nayak, S. Isolation and characterisation of nanofibrillated cellulose from waste cotton:effects on thermo-mechanical properties of polylactic acid/MA-g-SEBS blends. *Iranian Polymer Journal* **2019**, *28*. DOI: 10.1007/s13726-019-00733-3.
(50) Soni, B.; Hassan, E. B.; Mahmoud, B. Chemical isolation and characterization of different cellulose nanofibers from cotton stalks. *Carbohydrate Polymers* **2015**, *134*, 581-589. DOI: https://doi.org/10.1016/j.carbpol.2015.08.031.
(51) Severini, L.; De France, K. J.; Sivaraman, D.; Kummer, N.; Nyström, G. Biohybrid Nanocellulose–Lysozyme Amyloid Aerogels via Electrostatic Complexation. *ACS Omega* **2022**, *7* (1), 578-586. DOI: 10.1021/acsomega.1c05069.
(52) Zhang, F.; Ren, H.; Tong, G.; Deng, Y. Ultra-lightweight poly (sodium acrylate) modified TEMPO-oxidized cellulose nanofibril aerogel spheres and their superabsorbent properties. *Cellulose* **2016**, *23* (6), 3665-3676.
(53) Hu, J.; Tian, D.; Renneckar, S.; Saddler, J. N. Enzyme mediated nanofibrillation of cellulose by the synergistic actions of an endoglucanase, lytic polysaccharide monooxygenase (LPMO) and xylanase. *Scientific reports* **2018**, *8* (1), 1-8.
(54) Pottathara, Y. B.; Bobnar, V.; Grohens, Y.; Thomas, S.; Kargl, R.; Kokol, V. High dielectric thin films based on UV-reduced graphene oxide and TEMPO-oxidized cellulose nanofibres. *Cellulose* **2021**, *28* (5), 3069-3080.
(55) Schulze, M.; Reissner, R.; Lorenz, M.; Gülzow, E. Characterization of polymers in PEFC-electrodes with EDX and XPS. *Fresenius' journal of analytical chemistry* **1999**, *365* (1), 123-132.
(56) Gupta, B. D.; Semwal, V.; Pathak, A. Chapter 7 - Nanotechnology-based fiber-optic chemical and biosensors. In *Nano-Optics*, Thomas, S., Grohens, Y., Vignaud, G., Kalarikkal, N., James, J. Eds.; Elsevier, 2020; pp 163-195. Khanal, D.; Zhang, J.; Ke, W.-R.; Banaszak Holl, M. M.; Chan, H.-K. Bulk to nanometer-scale infrared spectroscopy of pharmaceutical dry powder aerosols. *Analytical Chemistry* **2020**, *92* (12), 8323-8332.
(57) Baer, D. R.; Artyushkova, K.; Brundle, C. R.; Castle, J. E.; Engelhard, M. H.; Gaskell, K. J.; Grant, J. T.; Haasch, R. T.; Linford, M. R.; Powell, C. J.; Shard, A. G.; Sherwood, P. M. A.; Smentkowski, V. S. Practical Guides for X-Ray Photoelectron Spectroscopy (XPS): First Steps in planning, conducting and reporting XPS measurements. *Journal of vacuum science & technology. A, Vacuum, surfaces, and films : an official journal of the American Vacuum Society* **2019**, *37*, 10.1116/1111.5065501. DOI: 10.1116/1.5065501 PubMed.
(58) Otter, L. M.; Förster, M. W.; Belousova, E.; O'Reilly, P.; Nowak, D.; Park, S.; Clark, S.; Foley, S. F.; Jacob, D. E. Nanoscale Chemical Imaging by Photo-Induced Force Microscopy: Technical Aspects and Application to the Geosciences. *Geostandards and Geoanalytical Research* **2021**, *45* (1), 5-27. Albrecht, T. R.; Nowak, D.; Morrison, W.; Park, S. Chemical Mapping at the Nanoscale by Photo-induced Force Microscopy. Park, S.; Nowak, D.; Albrecht, T. Nanoscale Chemical Mapping of Semiconductor Devices and Materials via PiFM. In *ISTFA 2018*, 2018; ASM International: pp 330-333.

(59) Goormaghtigh, E. Infrared Spectroscopy: Data Analysis. In *Encyclopedia of Biophysics*, Roberts, G. C. K. Ed.; Springer Berlin Heidelberg, 2013; pp 1049-1057.
(60) Haris, P. I. Infrared Spectroscopy of Protein Structure. In *Encyclopedia of Biophysics*, Roberts, G. C. K. Ed.; Springer Berlin Heidelberg, 2013; pp 1095-1106.
(61) Gaharwar, A. K.; Peppas, N. A.; Khademhosseini, A. Nanocomposite hydrogels for biomedical applications. *Biotechnology and bioengineering* **2014**, *111* (3), 441-453.